Acta Mech 236, 153–171 (2025)
https://doi.org/10.1007/s00707-024-04110-x

ORIGINAL PAPER

Ferruh Turan · **Muhammed Fatih Basoglu** · **Vu Ngoc Viet Hoang**

Lateral torsional stability of porous thin-walled I-beams with nonuniform porosity distributions subjected to a uniformly distributed load

Received: 12 July 2024 / Revised: 17 August 2024 / Accepted: 6 September 2024 / Published online: 12 November 2024
© The Author(s), under exclusive licence to Springer-Verlag GmbH Austria, part of Springer Nature 2024

Abstract Existing pores play a significant role in structural materials used in structural members such as plates, shells, and beams. Numerous qualities expected from structural materials involving the lightweight, high stiffness-to-weight ratio, high strength-to-weight ratio, resistance to mechanical and thermal shocks, and thermal insulation can be satisfied by setting porosity distribution from one surface to another. The porosity distribution affects the Young's modulus, shear modulus, and mass density of the material. However, there is a lack of study on the lateral-torsional buckling (LTB) behavior of porous orthotropic thin-walled beams with I-sections. To remedy this lack, this paper aims to analyze the lateral-torsional buckling (LTB) behavior of porous orthotropic thin-walled beams with I-sections subjected to a uniformly distributed load. Young's modulus, shear modulus, and mass density are assumed to be varied in the height direction according to four different porosity distribution patterns. The governing differential equation system of the LTB problem, including the equation of the warping effect, is developed using the Virtual work principle based on classical beam theory. Galerkin's method and an auxiliary function of simply supported boundary conditions are employed to obtain critical LTB load formulation. Additionally, the formulation is confirmed via comparing with existing literature. A parametric study is applied to investigate the influences of porosity coefficients, porosity distribution patterns, orthotropy, slenderness ratio, and geometrical characteristics on the LTB characteristics of porous beams. Parametric study indicates that critical LTB loads of orthotropic I-beams reduce as the web depth and porosity coefficients increase, and they increase with an increase in the orthotropy ratio, flange slenderness ratio, flange-to-web thickness ratio, and span of the beam. The buckling loads of the beam with the D1 pattern are higher than its perfect (D4) counterpart, so the D1 porosity pattern is the best choice to improve the bearing capacity of orthotropic I-beams. Also, the nonuniform porosity distributions (D1 and D3) increasing from origin to flanges enhance the lateral stability of I-beams because the flange has the maximum Young's modulus. The novelty of this study lies in its comprehensive LTB investigation of orthotropic thin-walled beams with I sections exposed to specific effects, such as porosity and warping. These effects on the structural performance are highlighted to significant insights into the porous material design to improve engineering structures' LTB resistance. This study enhances our understanding of composite materials and their application in structural stability analysis across various engineering fields.

F. Turan (✉)
Faculty of Engineering, Ondokuz Mayis University, Samsun, Turkey
E-mail: ferruh.turan@omu.edu.tr

M. F. Fatih
Faculty of Engineering and Architecture, Tokat Gaziosmanpasa University, Tokat, Turkey

V. N. V. Hoang
Bach Khoa Phu Tho Technology Co., Ltd, Ho Chi Minh City, Viet Nam

1 Introduction

The thin-walled structural elements have been used in various engineering fields, such as steel structures, bridges, and airplane wings. This situation occurs because of their higher in-plane strength-to-weight and stiffness-to-weight ratios, architectural demand, and functional requirements. However, poor torsional strength and out-of-bending resistance are some handicaps for thin-walled beams with open or closed cross sections. Moreover, the thin-walled beams without rigid lateral supports can undergo LTB deformations at a value well below their ultimate flexural strength capacity. In summary, a laterally unbraced thin-walled beam subjected to initial bending around its major axis may suddenly undergo the flexural-torsional situation due to the above handicaps. So, the deformation changes from in-plane bending to the torsional bending. The result is that the LTB deformation model includes a lateral deformation and a cross-sectional torsion depending on the geometrical characteristics of the thin-walled cross section. Also, this torsion involves the warping effects of the cross section. The combination of bending and torsion (with warping) makes the behavior of thin-walled beams quite complex.

In recent years, the application of thin-walled beams with various cross sections has a significant interest in many engineering fields due to allowing the optimal design involving a high strength-to-weight ratio. With technological developments, thin-walled structural components of lightweight materials with desirable features such as high stiffness-to-weight ratio, high strength-to-weight ratio, and fatigue resistance have become increasingly common. Therefore, analyzing the LTB response of porous orthotropic thin-walled beams with I-section is necessary. A literature review is presented in the following paragraph with a short description of a few of them.

Based on the finite element simulation, Dahmani and Drizi [1] aimed to fill the gaps in the literature about design rules for eccentrically loading thin-walled beams with channel cross sections. Bedon and Amadio [2] presented a closed-form solution for the LTB behavior of laterally restrained glass beams to develop a standardized design method. Derks [3] presented a buckling tool to provide engineers with an accurate, simple, quick, and effective assessment of composite beams' lateral shear and buckling responses. Based on the FE test simulation, Subramanian et al. [4] tested the I-section member's LTB resistance to propose improvements to the current LTB resistance equation to estimate numerical values closer to the test results. Subramanian and White [5] performed a uniform bending test to analyze the sensitivity of LTB equations based on AASHTO and AISC for steel I-section members. Jönsson et al. [6] investigated the accuracy of the interaction methods for coupling effects of flexural and lateral torsional buckling using statistical data based on Eurocode interaction equations. Sahraei and Mohareb [7] presented an FE formulation to estimate the LTB capacity of plane frames with moment connections. They deduced that the solution agrees well with the shell-based FE solution for LTB resistance predictions. Fortan and Rossi [8] validated ANSYS's geometrical and material nonlinear model with the experimental steel beam's LTB response results. They also performed parametric studies to ensure the design safety of all stainless-steel families considered in civil engineering structures. Agüero et al. [9] proposed a method to predict the effects of initial imperfection on the LTB capacity of beams with doubly symmetric sections. Their method involved the Eurocode rules, considering the geometrical equivalent of Unique Global and Local Initial imperfections. Rossi et al. [10] aimed to investigate the effects of structural imperfections (residual stresses) on the LTB resistance of I-beams based on the post-buckling numerical analysis with ABAQUS software. Armouti [11] analyzed the LTB of elastic prismatic beams under general loading and boundary conditions using FEM analysis based on linear beam element formulations. de Carvalho et al. [12] aimed to fill the gaps in the literature with the investigation of global stability and LTB strength of I-beams made of sinusoidal web openings. They performed parametric studies for the LTB response of this beam type using ABAQUS, including initial imperfections. Soltani [13] analyzed the LTB behavior of thin-walled beams with tapered I-sections based on the classical laminated beam theory and Vlasov's assumptions. The author presented the influence of tapering ratios, transverse load position, and lamination schemes on the LTB resistance of laminated I-beams. Stroetmann and Fominow [14] investigated to the calibration of imperfections such as geometrical imperfections and residual stress for standardization proposal of a LTB strength based on Eurocodes. Belaid et al. [15] proposed an analytical formulation of the critical LTB moment of unstrained steel beams subjected to asymmetrical loading. Düğenci [16] studied to determine all irregular displacements in high-web beams caused by LTB effects using an image processing technique. The author detected the deformations and displacements caused by LTB effects with an accuracy of 99. For analyzing the LTB response of corrugated web girders, Pandit et al. [17] proposed a homogenization scheme based on strain-energy phenomena to convert corrugated sections into equivalent flat sheets using FE model.

The literature review deduces many investigations about the buckling and vibration responses of the porous beams with various cross sections [18–31]. Many investigations in the literature presented the effect of porosity, elastic foundation, electric and magnetic potential, graphene nanocomposites, volume fraction index, thermo-mechanical and geometrical characteristics on the bending, buckling, post-buckling and vibration responses of FG porous beams based on the shear deformation theories [32–45]. Li and Zhang [46] investigated the buckling and post-buckling response of FG porous nanobeams under the follower force, including surface effects such as surface stiffness and surface residual stress. They used symmetrical and asymmetrical porosity distribution models to grade the porous material properties in the thickness direction. Phan and Nguyen [47] proposed a new higher-order beam theory to analyze FG porous beams' free vibration and buckling with varying mechanical characteristics along the thickness depending on the three typical porosity distributions. Turan and Adiyaman [48] presented the influence of boundary conditions, graduation index, porosity coefficients, porosity patterns, and slenderness on the buckling sensitivity of bi-directional FG porous beams using higher-order finite element model based on parabolic shear deformation theory. Wang and Li [49] studied the thermoelastic dynamic responses of FG porous beams consisting of two porosity distribution patterns exposed to three thermal and wet conditions. Zhang and Sun [50] aimed to analyze the buckling and nonlinear post-buckling behaviors of bi-directional porous beam under bi-directional hygrothermal loadings using Euler–Bernoulli beam theory involving the von-Karman nonlinear assumptions. Song and She [51] investigated the nonlinear vibrations and chaotic dynamic behaviors of rotating graphene platelets reinforced metal foams with three different distribution patterns of graphene platelets under thermal loadings. They used Runge–Kutta and multi-scale methods to analyze the amplitude-frequency response, bifurcation curve, and chaotic motion of the rotating blades. Zhang and She [52] analyzed the combined resonances of spinning cylindrical shells subjected to multi-source excitation using Reddy's higher-order shear deformation theory. They presented some numerical analyses to show the influence of different parameters on the combined resonances and chaos motions.

There is a lack of study in the existing literature addressing the LTB characteristics of beams or arches made of porous materials. Under thermos-mechanical loads, Ziane et al. [53] proposed a new formula for critical LTB moment of box beams with varying material properties along the wall thickness based on a power law rule. Liu et al. [54] presented the effects of porosity coefficients, porosity patterns, graphene platelets' weight parameter, load position, and slenderness ratio on the LTB capacity of FG porous circular arches reinforced with graphene platelets exposed to an arbitrary radial concentrated load. Therefore, the literature review shows that the LTB analysis of orthotropic porous beams has not been reported yet despite its practical importance.

Because of the application of composite structural members with thin-walled cross sections made of lightweight materials such as porous materials in the various engineering fields, especially aircraft, high-speed trains, etc, it is necessary to analyze the porous orthotropic thin-walled beams with I section. In the field of aerospace engineering, for instance, there is an ongoing effort to reduce the weight of structural elements while simultaneously enhancing their strength and stability. The implementation of this process is of paramount importance for the improvement of fuel efficiency, an increase in payload capacity, and an overall enhancement of the vehicle's performance. Due to their favorable strength-to-weight ratio, thin-walled structures such as I-beams have become a prevalent material for the construction of aircraft fuselages, wings, and other critical components.One of the primary challenges encountered in the design of these thin-walled structures is that of ensuring their stability under various loading conditions, such as uniform distributed loads. These loads have the potential to induce lateral-torsional buckling, a failure mode characterized by the twisting and bending of a beam in a lateral direction, which could result in a catastrophic failure. Such risks are compounded in porous orthotropic materials, which are frequently employed in aerospace applications due to their tailored mechanical properties and reduced weight.

The methodology outlined in this study on the lateral-torsional buckling response of porous orthotropic thin-walled I-beams subjected to a uniformly distributed load can be effectively employed in the design of lightweight aerospace components. A comprehensive understanding of the influence of porosity distribution and orthotropic material properties on buckling behavior allows engineers to optimize the design of I-beams used in aircraft structures. This optimization could involve:

- Selecting the appropriate porous orthotropic materials with tailored properties to enhance stability while minimizing weight.
- The design of I-beams with specific porosity distributions serves to delay the onset of lateral-torsional buckling, thereby increasing the safety margin.
- The utilization of derived analytical models for the simulation and prediction of buckling behavior in new materials and designs prior to physical testing facilitates a reduction in development time and associated costs.

The knowledge obtained from this investigation could facilitate the advancement of more productive and secure aerospace structures, thereby contributing to the evolution of lightweight materials within the industry. By implementing these findings, engineers can develop more effective designs that meet the rigorous standards of aerospace and other engineering applications.

However, there is a lack of study on the lateral-torsional buckling (LTB) behavior of porous orthotropic thin-walled beams with I-sections. To remedy this lack, this paper focuses on analyzing the LTB sensitivity of porous orthotropic double-symmetric I-beams with various porosity distribution patterns. The governing equations involving axial, vertical, and lateral deformations, twisting angle, and warping effects are developed using the Virtual work principle based on the classical beam theory. After some mathematical process, the governing equation is obtained only regarding the twisting angle. The governing differential equation can be solved using Galerkin's method and an auxiliary function satisfying the simply supported boundary condition, and then the LTB formulation is obtained. The acquired formulation can be applied to estimating porous orthotropic I-beams' critical LTB load values. Our results are compared with those in the existing literature to confirm the accuracy and efficiency of the obtained formulation, and a good agreement is observed. A parametric study is presented to estimate the effects of porosity coefficients, porosity patterns, orthotropy, warping parameters, slenderness ratio, and geometrical characteristics on the critical LTB load values of porous orthotropic thin-walled I-beams exposed to a uniformly distributed load.

2 Theoretical formulations

2.1 Geometrical description of I-beams and kinematics relations

This study focuses on the lateral-torsional buckling (LTB) analysis of an orthotropic I-beam with various porosity distribution patterns. Figure 1 indicates the Cartesian coordinate system with the x-axis along the longitudinal direction, y-axis in the lateral direction, and z-axis along the vertical direction. The origin of these axes (O) is located at the centroid of the doubly symmetric I-section. The symmetrically porous orthotropic I-beam is initially subjected to a laterally distributed load q. Figure 1 also shows the cross section of the beam with the height h, the flange width b, the flange thickness t_f and the web width t_w.

This study considers the nonuniform torsion model based on the classical beam theory for describing the displacement field of a point on the section. This beam theory assumes that the beams are slender and long

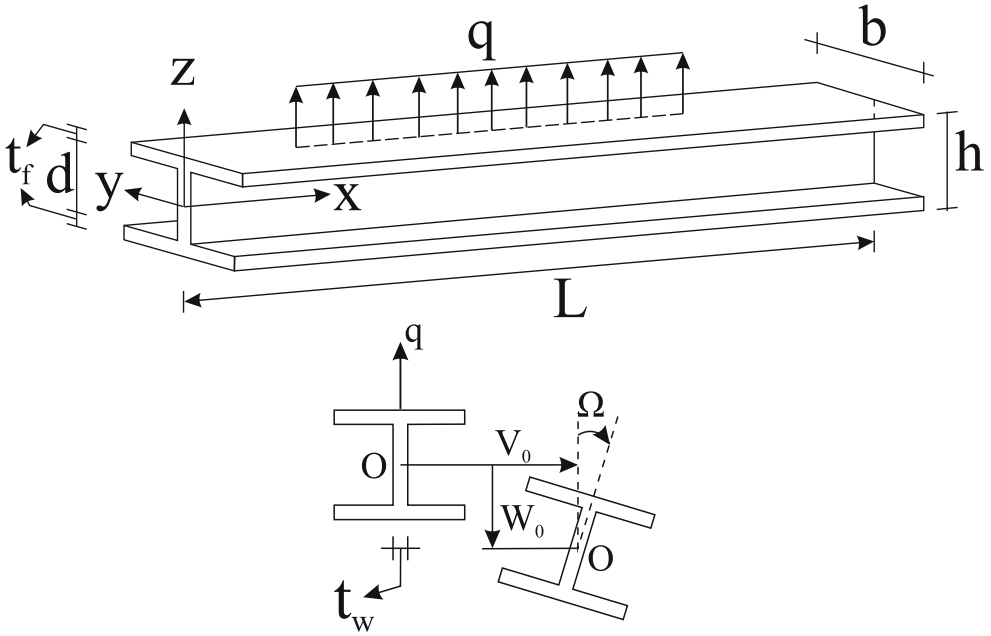


Fig. 1 Geometrical configuration for doubly symmetric I-beam subjected to a uniformly distributed loading and view of lateral-torsional deformation of cross section

and there are no shear deformations in the surface of the section. Also, it is admitted that the cross section does not change shape during deflection. These assumptions mean the cross section is rigid in its plane, so no distortional deformation occurs. So, the beam's deformation can be described as three distinct motions: (i) an axial displacement $U(x, y, z)$ in the x direction, (ii) a lateral displacement $V(x, y, z)$ in the y direction, (iii) a vertical displacement $W(x, y, z)$ in the z direction. From these assumptions, the displacement fields for an arbitrary point on the beam can be determined as follows [13,55–57]:

$$\begin{aligned} U(x, y, z) &= U_0(x) - y\frac{dV_0(x)}{dx} - z\frac{dW_0(x)}{dx} - \psi(y, z)\frac{d\Omega(x)}{dx} \\ V(x, y, z) &= V_0\ (x) - z\Omega(x) \\ W(x, y, z) &= W_0\ (x) + y\Omega(x) \end{aligned} \tag{1}$$

where Ω is the twisting angle, the cross section's rotation is a linear function of the axial coordinate. U_0, V_0, and W_0 are the displacement components of the reference point O. The term $\psi(y, z)$ is the out-of-plane displacement, called the warping function, which can depend on the y and z coordinates. It can be expressed as follows [54]:

$$\psi(y, z) = \begin{cases} yz & \text{for upper flange} \\ -yz & \text{for web} \\ yz & \text{for bottom flange} \end{cases} \tag{2}$$

Strain–displacement relations in a Cartesian coordinate can be expressed as follows:

$$\begin{aligned} \varepsilon_x &= \frac{\partial U}{\partial x},\ \varepsilon_y = \frac{\partial V}{\partial y},\ \varepsilon_z = \frac{\partial W}{\partial z} \\ \gamma_{xy} &= \frac{\partial U}{\partial y} + \frac{\partial V}{\partial x},\ \gamma_{xz} = \frac{\partial U}{\partial z} + \frac{\partial W}{\partial x},\ \gamma_{yz} = \frac{\partial V}{\partial z} + \frac{\partial W}{\partial y} \end{aligned} \tag{3}$$

in which ε_i and γ_{ij} are normal and shear strains, respectively. Substituting Eq. (1) into Eq. (3) gives the following strain relations:

$$\begin{aligned} \varepsilon_x =& \frac{dU_0}{dx} - y\frac{d^2V_0}{dx^2} - z\frac{d^2W_0}{dx^2} - \psi\frac{d^2\Omega}{dx^2}, \gamma_{xy} = -\left(z + \frac{d\psi}{dy}\right)\frac{d\Omega}{dx}, \gamma_{xz} = \left(y - \frac{d\psi}{dz}\right)\frac{d\Omega}{dx} \\ \varepsilon_y =& \varepsilon_z = \gamma_{yz} = 0 \end{aligned} \tag{4}$$

2.2 The material properties of the porous orthotropic I-beams

This paper considers four types of porosity distribution: a uniform porosity distribution (UD) and three nonuniform porosity distributions (D1, D2, and D3). D1 corresponds to a symmetrical distribution with decreasing stiffness from the cross section's surface to the origin. D2 represents a symmetrical distribution containing increasing stiffness from the cross section's surface to the origin. D3 denotes asymmetric distribution

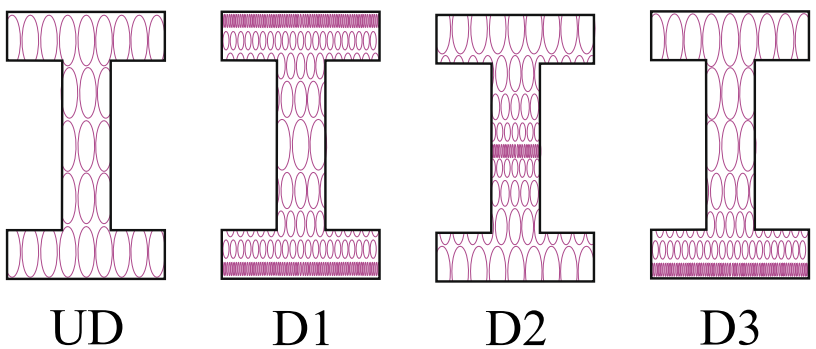


Fig. 2 Configuration of the UD, D1, D2, and D3 porosity distribution patterns on the cross section of the I-beam

with increasing stiffness from the cross section's top surface to the bottom surface (as illustrated in Fig. 2). $e_0 = e_m = 0$ means perfect material properties, which D4 represents through this paper.

Assuming that the material properties of the beam vary through the height direction of the beam's section, Young's modulus E, shear modulus G, and density ρ of porous beams are described as follows:

- for D1

$$(E, G_{xy}, G_{xz}, \rho) = (E_0, G_{0xy}, G_{0xz}, \rho_0)\left[1 - (e_0, e_0, e_0, e_m)\cos\left(\frac{\pi z}{h}\right)\right] \tag{5}$$

- for D2

$$(E, G_{xy}, G_{xz}, \rho) = (E_0, G_{0xy}, G_{0xz}, \rho_0)\left[1 - (e_0, e_0, e_0, e_m)\sin\left(\frac{\pi |z|}{h}\right)\right] \tag{6}$$

- for D3

$$(E, G_{xy}, G_{xz}, \rho) = (E_0, G_{0xy}, G_{0xz}, \rho_0)\left[1 - (e_0, e_0, e_0, e_m)\frac{3.45}{\pi}\sin\left(\frac{\pi z}{h}\right)\right] \tag{7}$$

- for UD

$$(E, G_{xy}, G_{xz}, \rho) = (E_0, G_{0xy}, G_{0xz}, \rho_0)(\overline{e}_0, \overline{e}_0, \overline{e}_0, \overline{e}_m) \tag{8}$$

where E_0, G_{0xy}, G_{0xz}, and ρ_0 are the porosity-independent material properties. e_0 and e_m are porosity coefficients of modulus and density, respectively. The porosity coefficients can be determined as $e_0 = 1 - E_1/E_0 = 1 - G_1/G_0$ and $e_m = 1 - \rho_1/\rho_0$ in the range of $0 \leq \{e_0, e_m\} < 1$. The typical mechanical properties of porous material can be described based on density as follows [53-56]:

$$E_1 = E_0\left(\frac{\rho_1}{\rho_0}\right)^2 \tag{9}$$

The relationship between the porosity coefficients for the UD pattern can be obtained as follows using Eq. (9):

$$\overline{e}_m = \sqrt{\overline{e}_0} \tag{10}$$

The masses of porous beam section with UD and D1 patterns are set to be equal as

$$\int_0^{0.5h} \sqrt{\overline{e}_0}\, dz = \int_0^{0.5h} \sqrt{1 - e_0 \cos\left(\frac{\pi z}{h}\right)}\, dz \tag{11}$$

The porosity parameter calculated by solving Eq. (11) can be estimated using the following relation:

$$\overline{e}_0 = 1 - 0.3194e_0^6 + 0.6869e_0^5 - 0.6058e_0^4 + 0.2313e_0^3 - 0.0697e_0^2 - 0.6336e_0 \tag{12}$$

A significant relationship exists between the beam's bearing capacity and Young's modulus. Therefore, examining Young's modulus distribution along the section for various porosity distributions is important. Figure 3 illustrates Young's modulus variation along the section height for four distinct types of porosity distribution.

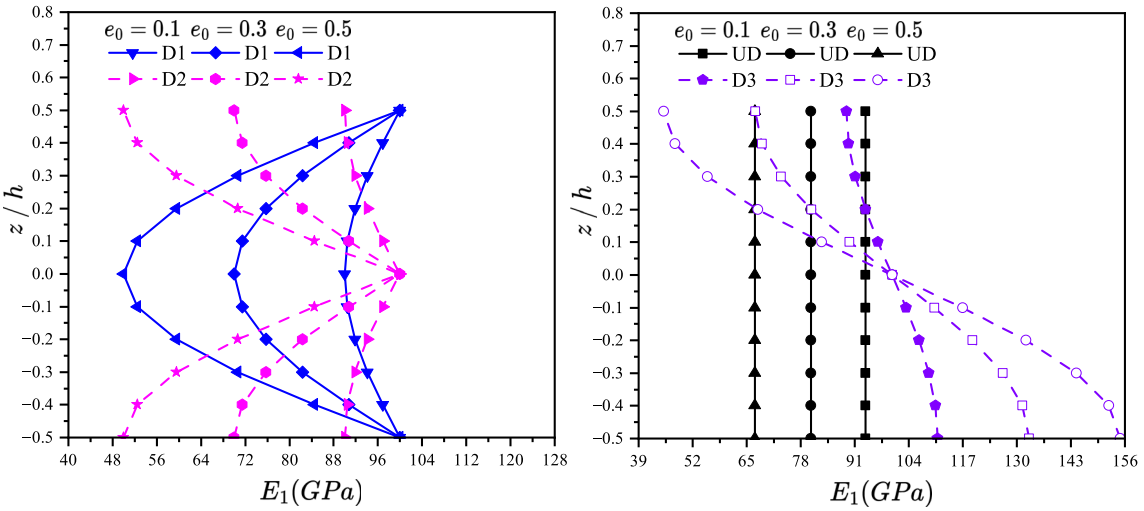


Fig. 3 Variation of Young's modulus through the section height

2.3 Stress–strain relations

Based on Hooke's law, we can write the stress–strain relations of a porous orthotropic I-beam as follows [13,55–57]:

$$\sigma_x = Q_{11}(z)\varepsilon_x,\ \tau_{xy} = Q_{66}(z)\gamma_{xy},\ \tau_{xz} = Q_{55}(z)\gamma_{xz} \tag{13}$$

in which

$$Q_{11}(z) = \frac{E(z)}{1-\nu_{12}\nu_{21}},\ Q_{55}(z) = G_{xz}(z),\ Q_{66}(z) = G_{xy}(z) \tag{14}$$

Substituting Eq. (4) into Eq. (13), the stress–strain relations can be obtained as:

$$\begin{aligned}
\sigma_x &= Q_{11}(z)\left[\frac{dU_0}{dx} - y\frac{d^2V_0}{dx^2} - z\frac{d^2W_0}{dx^2} - \psi\frac{d^2\Omega}{dx^2}\right]\\
\tau_{xy} &= -Q_{66}(z)\left[\left(z + \frac{d\psi}{dy}\right)\right]\frac{d\Omega}{dx}\\
\tau_{xz} &= Q_{55}(z)\left[\left(y - \frac{d\psi}{dz}\right)\right]\frac{d\Omega}{dx}
\end{aligned} \tag{15}$$

2.4 Virtual work principle for a porous orthotropic I-beam

We can obtain the constitutive equations of the porous beam's LTB problem using the Virtual work principle. The imperative is to ascertain the critical load at which the overall potential energy of the buckled system attains a stationary state. The analysis presupposes that the ultimate deformation encompasses three primary components: horizontal displacement, vertical displacement, and rotational displacement. The deformation process unfolds in a dual-stage manner, wherein the initial stage involves bending the beam in the vertical plane. Subsequently, upon reaching the critical load, the beam undergoes simultaneous torsional and lateral bending deformations. Accordingly, the equilibrium equations for the beam's LTB problem are derived from the Virtual work principle given by [13,54–57]:

$$\delta(U_s - W_e) = 0 \tag{16}$$

δ is the variation term. U_s represents the elastic strain energy, W_e expresses the work done by applied loads. So, the variation in porous orthotropic I-beam's strain energy can be reduced to the following terms:

$$\delta U_s = \int_0^L \int_A (\sigma_x \delta\varepsilon_x + \tau_{xy}\delta\gamma_{xy} + \tau_{xz}\delta\gamma_{xz})dAdx \tag{17}$$

in which L and A correspond to the beam's length and the cross-sectional area. Substituting Eq. (4) into Eq. (17), the following equation can be obtained:

$$\delta U_s = \int_0^L \int_A \left(\sigma_x \left[\frac{d\delta U_0}{dx} - y\frac{d^2\delta V_0}{dx^2} - z\frac{d^2\delta W_0}{dx^2} - \psi\frac{d^2\delta\Omega}{dx^2} \right] + \tau_{xy}\left[\left(z + \frac{d\psi}{dy} \right) \frac{d\delta\Omega}{dx} \right] + \tau_{xz}\left[\left(y - \frac{d\psi}{dz} \right) \frac{d\delta\Omega}{dx} \right] \right) dA dx \quad (18)$$

Performing integration for Eq. (18), we have the variation of strain energy formulated in terms of stress resultants acting on the cross-sectional area of the elastic beam in the buckled configuration as follows:

$$\delta U_s = \int_0^L \left(N_x \frac{d\delta U_0}{dx} - M_y \frac{d^2\delta W_0}{dx^2} + M_z \frac{d^2\delta V_0}{dx^2} + M_\psi \frac{d^2\delta\Omega}{dx^2} + M_{st}\frac{d\delta\Omega}{dx} \right) dx \quad (19)$$

in which

$$\begin{aligned} N_x &= \int_A \sigma_x dA, \quad M_y = \int_A z\sigma_x dA, \quad M_z = -\int_A y\sigma_x dA, \quad M_\psi = -\int_A \psi\sigma_x dA \\ M_{st} &= \int_A \left[\tau_{xz}\left(y - \frac{d\psi}{dz} \right) - \tau_{xy}\left(z + \frac{d\psi}{dy} \right) \right] dA \end{aligned} \quad (20)$$

where N_x is the axial force. M_y and M_z are the bending moments about major and minor axes, respectively. M_ψ is the warping moment due to the warping of the cross section. M_{st} is the St-Venant torsion moment. Based on the classical beam theory, the stress resultants are derived in terms of displacement components by substituting Eq. (15) into Eq. (20) as follows:

$$\begin{aligned} N_x &= A_1\frac{dU_0}{dx} - B_1\frac{d^2V_0}{dx^2} - B_2\frac{d^2W_0}{dx^2} - C_1\frac{d^2\Omega}{dx^2} \\ M_y &= A_2\frac{dU_0}{dx} - B_3\frac{d^2V_0}{dx^2} - B_4\frac{d^2W_0}{dx^2} - C_2\frac{d^2\Omega}{dx^2} \\ M_z &= -A_3\frac{dU_0}{dx} + B_5\frac{d^2V_0}{dx^2} + B_6\frac{d^2W_0}{dx^2} + C_3\frac{d^2\Omega}{dx^2} \\ M_\psi &= -A_4\frac{dU_0}{dx} + B_7\frac{d^2V_0}{dx^2} + B_8\frac{d^2W_0}{dx^2} + C_4\frac{d^2\Omega}{dx^2} \\ M_{st} &= (C_5 + C_6)\frac{d\Omega}{dx} \end{aligned} \quad (21)$$

In this equation, A_1 denotes axial stiffness. $B_i (i = 1..6)$ represents the flexural stiffness of y- and z-axes. $C_i (i = 1..4)$ is warping and $C_i (i = 5, 6)$ torsional stiffness of porous orthotropic I-beam, defined by

$$\begin{aligned} A_1 &= b\int_{-0.5h}^{-0.5d} Q_{11}(z)dz + t_w\int_{-0.5d}^{0.5d} Q_{11}(z)dz + b\int_{0.5d}^{0.5h} Q_{11}(z)dz \\ A_2 = B_2 &= b\int_{-0.5h}^{-0.5d} zQ_{11}(z)dz + t_w\int_{-0.5d}^{0.5d} zQ_{11}(z)dz + b\int_{0.5d}^{0.5h} zQ_{11}(z)dz \\ B_4 &= b\int_{-0.5h}^{-0.5d} z^2Q_{11}(z)dz + t_w\int_{-0.5d}^{0.5d} z^2Q_{11}(z)dz + b\int_{0.5d}^{0.5h} z^2Q_{11}(z)dz \end{aligned} \quad (22)$$

$$\begin{aligned} B_5 &= \frac{b^3}{12}\int_{-0.5h}^{-0.5d} Q_{11}(z)dz + \frac{t_w^3}{12}\int_{-0.5d}^{0.5d} Q_{11}(z)dz + \frac{b^3}{12}\int_{0.5d}^{0.5h} Q_{11}(z)dz \\ B_7 = C_3 &= \frac{b^3}{12}\int_{-0.5h}^{-0.5d} zQ_{11}(z)dz + \frac{t_w^3}{12}\int_{-0.5d}^{0.5d} zQ_{11}(z)dz + \frac{b^3}{12}\int_{0.5d}^{0.5h} zQ_{11}(z)dz \\ C_4 &= \frac{b^3}{12}\int_{-0.5h}^{-0.5d} z^2Q_{11}(z)dz + \frac{t_w^3}{12}\int_{-0.5d}^{0.5d} z^2Q_{11}(z)dz + \frac{b^3}{12}\int_{0.5d}^{0.5h} z^2Q_{11}(z)dz \end{aligned} \quad (23)$$

$$
\begin{aligned}
C_5 &= \frac{t_w^3}{3}\int_{-0.5d}^{0.5d} Q_{55}(z)dz \\
C_6 &= 4b\int_{-0.5h}^{-0.5d} z^2 Q_{66}(z)dz + 4b\int_{0.5d}^{0.5h} z^2 Q_{66}(z)dz \\
A_3 &= A_4 = B_1 = B_3 = B_6 = B_8 = C_1 = C_2 = 0
\end{aligned}
\tag{24}
$$

This study assumes that a uniformly distributed load can be applied to the I-beam's centroid (shear center), and that the load remains vertical for the buckled beam's shape. The deformation of the beam occurs as follows: (i) it bends in the vertical plane, and (ii) it laterally buckles. The second case concerns estimating the energy of lateral buckling. $B_5\frac{d^2V_0}{dx^2} = \overline{M}_z$ can be written. $\overline{M}_z$ is the moment about the buckled beam's vertical axis. The value of the slope is obtained as $\frac{dV_0}{dx} = x\frac{\overline{M}_z}{B_5}$. Based on the sign conventions between the unbuckled and buckled beam's axes, it can be written as $\overline{M}_z = -\Omega M_y$. For uniformly distributed load conditions, the bending moment distribution through the x-axis is given by

$$
M_y = q\frac{L^2}{2}\left(\frac{x}{L} - \frac{x^2}{L^2}\right) \tag{25}
$$

The variation in the work of porous orthotropic I-beam is expressed by

$$
\delta W_e = \int_0^L \left(q^2\frac{L^4}{2}x\left(\frac{x}{L} - \frac{x^2}{L^2}\right)^2\frac{\Omega}{B_5}\delta\Omega\right)dx \tag{26}
$$

Substituting Eqs. (19) and (26) into Eq. (16), we have

$$
\begin{aligned}
&\int_0^L \left(N_x\frac{d\delta U_0}{dx} - M_y\frac{d^2\delta W_0}{dx^2} + M_z\frac{d^2\delta V_0}{dx^2} + M_\psi\frac{d^2\delta\Omega}{dx^2} + M_{st}\frac{d\delta\Omega}{dx}\right)dx \\
&- \int_0^L \left(q^2\frac{L^4}{2}x\left(\frac{x}{L} - \frac{x^2}{L^2}\right)^2\frac{\Omega}{B_5}\delta\Omega\right)dx = 0
\end{aligned}
\tag{27}
$$

The constitutive LTB equations can be derived through integration by parts and setting the coefficients of δU_0, δW_0, δV_0, and $\delta\Omega$ to zero, as outlined below:

$$
\begin{aligned}
&\frac{d^2N_x}{dx^2} = 0, \quad \frac{d^2M_y}{dx^2} = 0, \quad \frac{d^2M_z}{dx^2} = 0, \\
&\frac{d^2M_\psi}{dx^2} - \frac{dM_{st}}{dx} - q^2\frac{L^4}{2}x\left(\frac{x}{L} - \frac{x^2}{L^2}\right)^2\frac{\Omega}{B_5} = 0
\end{aligned}
\tag{28}
$$

Substituting Eq. (21) into Eq. (28), we can obtain the following set of constitutive equations for the LTB problem:

$$
A_1\frac{d^3U_0}{dx^3} - B_2\frac{d^4W_0}{dx^4} = 0 \tag{29a}
$$

$$
A_2\frac{d^3U_0}{dx^3} - B_4\frac{d^4W_0}{dx^4} = 0 \tag{29b}
$$

$$
B_5\frac{d^4V_0}{dx^4} + C_3\frac{d^4\Omega}{dx^4} = 0 \tag{29c}
$$

$$
B_7\frac{d^4V_0}{dx^4} + C_4\frac{d^4\Omega}{dx^4} - (C_5 + C_6)\frac{d^2\Omega}{dx^2} - q^2\frac{L^4}{2}x\left(\frac{x}{L} - \frac{x^2}{L^2}\right)^2\frac{\Omega}{B_5} = 0 \tag{29d}
$$

Substituting Eq. (29c) into Eq. (29d), we have

$$
\eta_1\frac{d^4\Omega}{dx^4} - \eta_2\frac{d^2\Omega}{dx^2} - q^2\frac{L^4}{2B_5}x\left(\frac{x}{L} - \frac{x^2}{L^2}\right)^2\Omega = 0 \tag{30}
$$

where

$$\eta_1 = C_4 - \frac{B_7 C_3}{B_5}, \quad \eta_2 = C_5 + C_6 \tag{31}$$

3 Solution of LTB problem

Since the resulting form of LTB equilibrium equations is only in terms of the twisting angle, the approximate lateral-torsional buckled shape of the beam must satisfy the essential simply supported boundary conditions for torsional rotation. For simply supported boundary conditions of I-beam, the twisting angle equals zero at both ends: $\Omega(0) = \Omega(L) = 0$. Furthermore, the I-beam's both ends are free to warp: $\left(\frac{d^2\Omega(0)}{dx^2}\right) = \left(\frac{d^2\Omega(L)}{dx^2}\right) = 0$. Therefore, the twisting angle becomes:

$$\Omega(x) = \Omega_1 \sin\left(\frac{m\pi x}{L}\right) \tag{32}$$

where Ω_1 is the arbitrary coefficients. m represents the number of half-waves in the x direction.

Galerkin's method is one of the most convenient solution techniques to estimate the critical LTB load values of different types of continuous structural elements. By substituting Eq. (32) into Eq. (30) and applying Galerkin's method, we obtain the following LTB load equation of q as follows:

$$q = 10.954\frac{m^3\pi^3}{L^3}\sqrt{\frac{B_5}{L^2}\left(\frac{\eta_2 L^2 + \eta_1 m^2\pi^2}{m^4\pi^4 + 45}\right)} \tag{33}$$

The LTB load of the beam depends on the parameter m, and the critical LTB load (q_{cr}) value can be obtained as the minimum value among these LTB loads.

4 Numerical results

In the previous section, an analytical methodology based on the virtual work principle has been formulated to estimate the critical LTB load values of the I-beam. This section presents a comprehensive parametric study to illustrate the effects of significant parameters, including porosity distribution patterns, porosity coefficients, orthotropy, and geometrical characteristics, on the LTB sensitivity of porous orthotropic I-beam. The evaluated LTB load is expressed in the non-dimensional form to enhance comprehension of the numerical results:

$$q_{nd} = \frac{q_{cr} L^3}{E_0 t_w h^3} \tag{34}$$

The following section is subdivided into two distinct subsections: the initial subsection focuses on verifying the proposed formulation. At the same time, the second one investigates the influence of the factors mentioned above on the LTB response of the porous orthotropic I-beam.

4.1 Verification studies

A comparison of critical LTB moments of an isotropic I-beam subjected to a uniformly distributed load is applied. The critical buckling moment values are compared with the results of Sapountzakis and Dourakopoulos [45] and Mohri et al. [36], as given in Table 1. For comparison, the case of a simply supported IPE300 beam with characteristics of $E_0 = 210\ GPa$, $G_0 = 80.77\ GPa$ and $L = 6\,m$ has been studied. The critical LTB moment is determined as follows:

$$m_{cr} = \frac{q_{cr} L^2}{8} \tag{35}$$

It can observed from Table 1 that critical buckling moment values obtained using the present investigation are in good agreement with the results of the given references.

A comparison is made between the critical LTB moment results provided by Eq. (35) and the results of Benyamina et al. [55] to achieve the accuracy and efficiency of the proposed analytical solution. For comparison in Table 2, the case of a simply supported I-beam with various geometrical characteristics and material properties of $E_0 = 210\ GPa$ and $\nu = 0.3$ has been considered.

Table 1 Comparison of critical LTB moment values of D4 isotropic IPE300-beam

Source	$m_{cr}\ (kNm)$
Sapountzakis and Dourakopoulos [57]	97.72
Mohri et al. [56]	98.20
Eurocode-3 [58]	94.07
Present	93.96

Table 2 Comparison of critical LTB moment values of D4 isotropic doubly symmetrical I-beam subjected to uniformly distributed load for various geometrical properties

$m_{cr}(kNm)$		Benyamina et al. [10]			Present
Geometrical properties $b_f \times t_f \times t_w \times h$ (mm)	L (mm)	Ritz method	Analytical method	FEM	Eq. (35)
150 × 12.7 × 9.4 × 450	6000	184.61	186.22	183.96	186.23
	9000	103.25	104.18	103.31	103.73
	12,000	71.50	72.16	71.36	71.67
190 × 14.6 × 9.4 × 450	6000	336.06	338.66	323.57	327.36
	9000	188.64	190.18	182.56	183.67
	12,000	130.89	132.03	126.44	127.44

4.2 Parametric studies

Specifically, a simply supported I-beam with various porosity distributions and a span of L subjected to a uniformly distributed load is considered for analysis. It is assumed that both flanges' widths are (b), the I-section web depth is (d), and the thickness of the web is (t_w) and both flanges' thickness are (t_f). The beam is made of orthotropic graphite/epoxy (T) with the following elastic properties:

$$E_0 = 131\ (GPa),\ G_{0xy} = 6.895\ (GPa), G_{0xz} = 6.205\ (GPa), \nu_{12} = 0.22, \nu_{21} = 0.017$$

where the fibers are parallel and perpendicular to x- and y- axes, respectively, the evaluated critical LTB moment is expressed in the non-dimensional form as follows:

$$m_{nd} = \frac{m_{cr} L^3}{E_0 t_w^2 h^4} \tag{36}$$

In the first LTB analysis, the effect of slenderness on the lateral buckling stability of simply supported I-beam is investigated. The beams are made of porous orthotropic material with various porosity distribution patterns. The beam's slenderness has been varied from 2 m to 12 m. It is assumed that both flanges are to be 190 mm wide (b), the I-section's web is 420.8 mm deep (d), and 9.4 mm thick (t_w), and both flanges' thickness (t_f) are equal to 14.6 mm.

In this case, Table 3 and Fig. 4 exhibit the influence of the porosity and span of the beam on the variation of the non-dimensional critical LTB moment values of the porous orthotropic I-beam. It is seen that the critical moment value increases with an increase in the span of the beam. The porous UD beam has lower critical LTB moment values than its perfect counterpart, and the porous D1 beam has higher critical LTB moment values than the perfect beam in the range of $L > 2$ m. This result indicates that considering porosity's nonuniform distribution as decreasing from origin to flanges can significantly improve the non-dimensional critical LTB moment values of porous orthotropic I-beam. The reduction in porosity toward the flanges means that the flanges have higher material stiffness than the web. Since the flanges are primarily responsible for resisting bending and lateral-torsional deformation, their enhanced stiffness directly improves the beam's resistance to buckling. With an increase in L from 2 m to 12 m at $e_0 = 0.6$, the porosity effect remains constant as (−39.5%) for the UD pattern and increases by (14.8%) for the D1 pattern. The porosity effect differences between the two porosity patterns increase from (14.9%) to (65.9%) with an increase in e_0 from 0.2 to 0.6.

The second analysis investigates the effect of the web depth on the lateral buckling sensitivity of a simply supported I-beam. The web depth has been varied from 350 mm to 750 mm. Both flanges' width and thickness are 190 mm and 14.6 mm, respectively; the web thickness is 9.4 mm, and the span of the beam is 10 m. Table 4

Table 3 Non-dimensional critical LTB moment value of porous orthotropic I-beams with various porosity distributions versus span of beams

Non-dimensional critical LTB moment, m_{nd}							
e_0	0.0	0.2		0.4		0.6	
L (mm)	D4	UD	D1	UD	D1	UD	D1
2	22.681	19.768	22.517	16.793	22.353	13.715	22.189
4	46.252	40.311	46.310	34.245	46.361	27.968	46.406
6	71.549	62.359	72.543	52.972	73.492	43.264	74.403
8	99.310	86.553	102.193	73.520	104.920	60.049	107.515
10	130.154	113.434	136.027	96.348	141.511	78.697	146.674
12	164.579	143.435	174.618	121.824	183.872	99.510	192.495

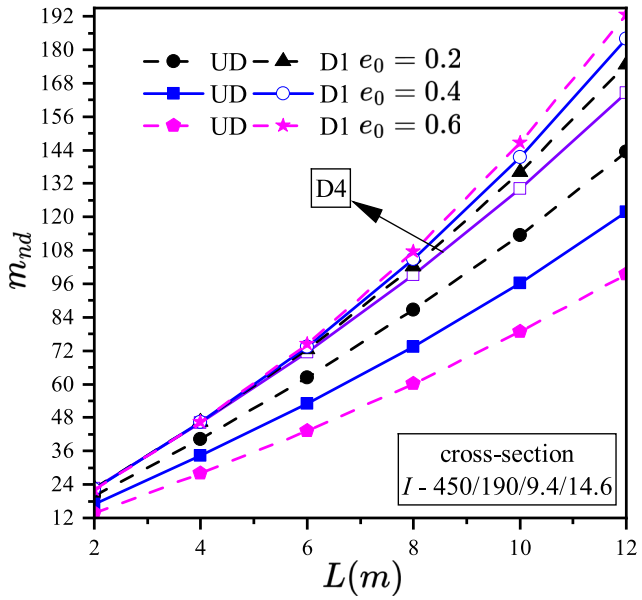


Fig. 4 Variation of non-dimensional critical LTB moment values of porous orthotropic I-beams with three porosity patterns versus span of beam

Table 4 Non-dimensional critical LTB moment value of porous orthotropic I- beams with various porosity distributions versus the web depth

Non-dimensional critical LTB moment, m_{nd}							
e_0	0.0	0.25		0.50		0.75	
d (mm)	D4	UD	D3	UD	D3	UD	D3
350	226.081	189.694	220.220	152.199	201.581	112.503	166.031
450	106.515	89.371	103.410	71.714	93.440	53.009	73.895
550	58.613	49.183	56.769	39.459	50.861	29.168	39.049
650	35.704	29.961	34.538	24.040	30.752	17.771	23.120
750	23.374	19.612	22.585	15.737	20.031	11.632	14.829

and Fig. 5 show the influences of the porosity coefficient, porosity distributions, and web depth (d) of the beam on the non-dimensional critical LTB moment values. It can be found from Table 4 and Fig. 5 that the critical LTB moment values of porous orthotropic I-beam with three porosity distribution patterns all decrease with an increase in d and e_0 parameters. When the d increases, the moment arm of twisting forces and warping effects increase due to increasing distance between the flanges. This larger moment arm amplifies the twisting effects when the beam is subjected to lateral-torsional buckling. Also, an increment in warping deformation reduces the critical LTB moment, as the beam's resistance to buckling is compromised. The perfect beam has the highest non-dimensional critical LTB moment, whereas the beam with the UD pattern has the lowest one. The

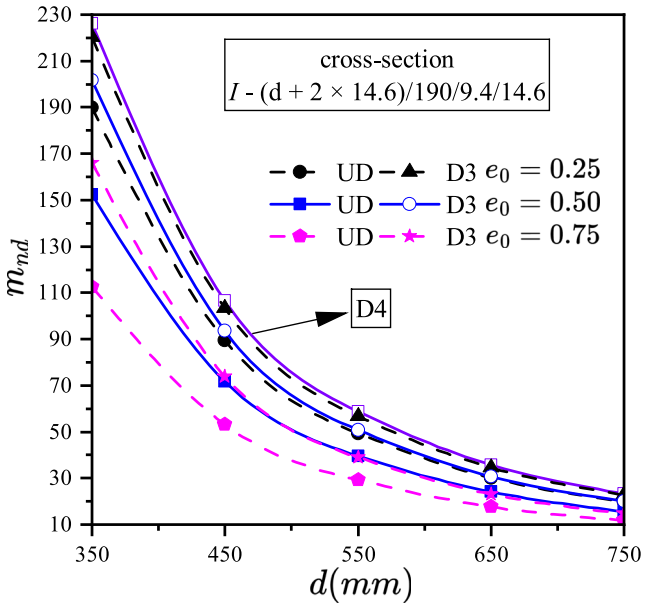


Fig. 5 Variation of non-dimensional critical LTB moment values of porous orthotropic I-beams with three porosity patterns versus the web depth

Table 5 Critical LTB load value of porous orthotropic I- beams with various porosity distributions versus flange-to-web thickness ratios

Critical LTB load, $q_{cr}(kN)$							
e_0	0.0	0.3		0.4		0.5	
t_f/t_w	D4	UD	D2	UD	D2	UD	D2
1.0	12.357	9.965	8.886	9.149	7.727	8.319	6.568
1.5	20.180	16.273	14.048	14.942	12.004	13.587	9.958
2.0	30.927	24.941	20.926	22.899	17.577	20.823	14.211
2.5	44.745	36.083	29.575	33.131	24.463	30.127	19.288
3.0	61.659	49.722	39.985	45.655	32.628	41.514	25.111
3.5	81.666	65.859	52.133	60.468	42.036	54.987	31.610
4.0	104.765	84.483	66.005	77.571	52.658	70.538	38.727

critical moment value differences between the beams with UD and D3 patterns are because at least a section with the D3 pattern flange has the maximum Young's modulus under the same parameters. The influence of porosity on the critical LTB moment values increases approximately (34%) with increasing e_0 from 0.25 to 0.75 at d=750 mm for both porosity distribution patterns. With an increase in d from 350 mm to 750 mm at e_0 = 0.75, the difference in porosity effect between UD and D3 patterns decreases from (47.6%) to (27.5%).

The third analysis focuses on the influence of the flange-to-web thickness ratio, an important parameter in the stability design of I-beams. The ratio has been adjusted within the range of 1 to 4. The span of the beam, the web thickness, the web depth, and both flanges width are selected as 12 m, 3.2 mm, 650 mm, and 190 mm, respectively. Table 5 and Fig. 6 display the variation of the critical LTB load values of porous orthotropic I-beam considering the change in flange-to-web thickness ratios and porosity coefficients. It can be seen that the critical LTB loads increase with the increase of the flange-to-web thickness ratio. The reason is that a higher ratio results in greater torsional stiffness and moment of inertia, making the beam more resistant to torsional deformation and tending to enhance the beam's stability against lateral-torsional buckling. The porous UD beam has lower critical LTB moment values than its perfect counterpart and higher critical LTB moment values than the D2 beam. This result indicates that considering nonuniform porosity distribution as decreasing from flanges to web can significantly reduce the critical LTB load values of porous orthotropic I-beam. The porosity decreases from the flanges to the web in the D2 beam compared to the UD beam. It means that the flanges, which are crucial in resisting both bending and torsional forces, have higher porosity (and thus lower torsional and bending stiffness) compared to the web. Since the flanges play a dominant role in resisting lateral-torsional

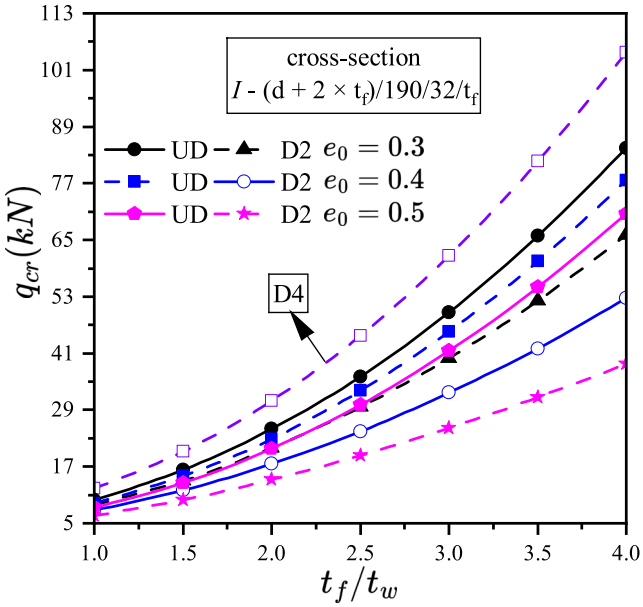


Fig. 6 Variation of critical LTB load values of porous orthotropic I-beams with three porosity patterns versus flange-to-web thickness ratios

Table 6 Critical LTB load value of porous orthotropic I- beams with various porosity distributions versus orthotropy ratios

Critical LTB load, $q_{cr}(kN)$							
e_0	0.0	0.2		0.4		0.6	
G_{xy}/G_{xz}	D4	UD	D1	UD	D1	UD	D1
2	5.735	4.998	6.114	4.247	6.462	3.468	6.785
4	6.450	5.621	7.153	4.776	7.782	3.900	8.353
6	7.095	6.184	8.062	5.252	8.907	4.288	9.669
8	7.681	6.698	8.878	5.688	9.910	4.645	10.826
10	8.234	7.174	9.624	6.094	10.817	4.976	11.869
12	8.741	7.617	10.311	6.476	11.651	5.285	12.828
14	9.225	8.042	10.966	6.830	12.435	5.580	13.725
16	9.690	8.448	11.574	7.168	13.166	5.857	14.562

buckling, their reduced stiffness severely compromises the beam's ability to resist such buckling, leading to a significantly lower critical LTB moment. With increase in t_f/t_w the ratio from 1 to 4 at $e_0 = 0.5$, the porosity effect remains constant as (−39.5%) for the UD pattern and increases from (−46.9%) to (−63.03%) for the D2 pattern. The porosity effect differences between the two porosity patterns increase by (24%) with an increase in e_0 from 0.3 to 0.5, and it increases by (17%) with increasing t_f/t_w the ratio from 1 to 4 at $e_0 = 0.4$.

The beam section's flexural and torsional stiffness influences the I-beams' LTB response. In an orthotropic material, these stiffnesses can vary in different directions and affect the overall behavior of the beam. For this reason, the next analysis is conducted to exhibit the orthotropy effect on the LTB response of porous I-beams. The orthotropy ratio (G_{xy}/G_{xz}) has been varied from 2 to 16. The span of the beam, web thickness, web depth, flanges thickness, and width are selected as 10 m, 9.4 mm, 470.8 mm, 14.6 mm, and 190 mm, respectively. The critical LTB load values versus the orthotropy ratio are presented in Table 6 and Fig. 7 for various porosity distribution patterns. It can be found from Table 6 and Fig. 7 that the critical LTB loads of the beam increase as the orthotropy ratio increases. This means that a higher orthotropy ratio leads to a greater shear stiffness difference between the orthogonal planes, and the variation in this ratio can result in variations in torsional stiffness, which indirectly affects the LTB response of I-beams. The critical LTB load values difference among the beams with three porosity distribution patterns becomes more significant. With increasing e_0 from 0.2 to 0.6 at $G_{xy}/G_{xz} = 16$, the effect of porosity on the critical LTB load values increases by (37.5%) and (26.7%) for D1 and UD patterns, respectively. Depending on the increasing G_{xy}/G_{xz} from 2 to 16 at $e_0 = 0.4$, the difference in porosity effect between UD and D1 patterns increases from (52.2%) to (83.7%).

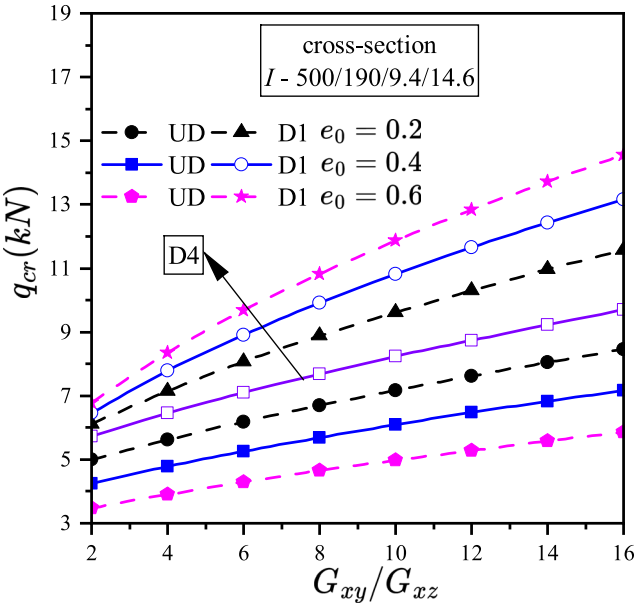


Fig. 7 Variation of critical LTB load values of porous orthotropic I-beams with three porosity patterns versus orthotropy ratios

Table 7 Critical LTB moment value of porous orthotropic I- beams with various porosity distributions versus flange slenderness ratios

Critical LTB moment, $m_{cr}(kNm)$							
e_0	0.0	0.3		0.6		0.9	
b/t_f	D4	UD	D3	UD	D3	UD	D3
10	23.060	18.590	22.383	13.941	20.233	8.769	16.014
12	36.568	29.495	35.298	22.113	31.181	13.911	22.709
14	54.894	44.268	52.748	33.195	45.737	20.877	30.659
16	78.832	63.572	75.507	47.673	64.507	29.982	39.941
18	109.236	88.092	104.345	66.046	88.133	41.551	50.605
20	146.866	118.428	140.025	88.810	117.180	55.854	62.762
22	192.557	155.283	183.330	116.446	152.296	73.229	76.413
24	247.137	199.305	235.002	149.460	194.103	93.994	91.772
26	311.374	251.094	295.825	188.300	243.199	118.424	108.810

The flange width-to-flange thickness, namely the flange slenderness ratio, can affect the LTB sensitivity of I-beams. In the stability analysis of I-beams, controlling the flange slenderness ratio is crucial to ensure that the I-beam can improve load-carrying capacity without lateral buckling failure. The following analysis focuses on the flange slenderness ratio effect to prove the importance of this ratio on the LTB stability of porous orthotropic I-beams. The ratio has been adjusted within the range of 10 to 24. The span of the beam, web thickness, web depth, and both flanges thickness, are considered as 12 m, 9.4 mm, 420.8 mm, and 14.6 mm, respectively. The influence of the flange slenderness ratio and porosity on the critical LTB moment values of porous orthotropic I-beams is displayed in Table 7 and Fig. 8. It can be seen that the critical LTB moments increase as the flange slenderness ratio increases. When the flange slenderness ratio increases relative to its thickness, the flanges help distribute stresses more evenly across the cross section, reducing warping deformation and differential twisting between the web and the flanges. Therefore, a higher flange slenderness ratio means that greater torsional and lateral bending stiffness and a greater proportion of the load are carried by the flanges, which are more effective at resisting bending and lateral-torsional deformations. This enhanced load-carrying capacity and stiffness allow the beam to withstand greater moments before reaching the critical buckling condition. With an increase in the b/t_f ratio from 10 to 26 at $e_0 = 0.9$, the porosity effect remains constant as (-62%) for the UD pattern and increases from (−30.56%) to (−65.1%) for the D3 pattern. The porosity effect differences between the two porosity patterns increase by (43.6%) with the increase in e_0 from 0.3 to 0.9, and it diminishes by (16%) with increasing the b/t_f ratio from 10 to 26 at $e_0 = 0.6$.

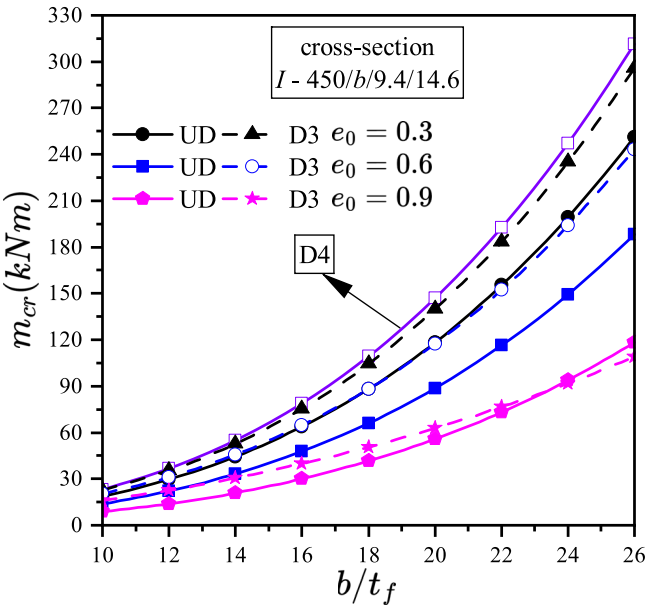


Fig. 8 Variation of critical LTB moment values of porous orthotropic I-beams with three porosity patterns versus flange slenderness ratios

5 Conclusion

The lateral-torsional buckling (LTB) of thin-walled I-beams is a crucial phenomenon in structural engineering. It occurs when the beam is simultaneously subjected to lateral displacement and torsional rotation. Dealing with the LTB behavior of thin-walled I-beams is crucial for ensuring structural stability, safety, and economical designs. For this reason, this paper deals with the LTB responses of porous orthotropic double-symmetric I-beams with various porosity distribution patterns subjected to a uniformly distributed load. Virtual work principles derive the governing equations, which are solved using Galerkin's method to obtain LTB formulation. A parametric study is conducted to assess the effects of porosity coefficients, porosity patterns, orthotropy, and some crucial parameters such as span of beam, web depth, flange slenderness ratio, and flange-to-web thickness ratio on the critical LTB loads of porous orthotropic thin-walled I-beams. This research contributes to composite materials and structural stability analysis, presenting potential applications across various engineering domains. Several noticeable remarks of the present study are as follows:

1. The critical LTB load values for the beam with D1 and D3 patterns are higher than those observed for the beam with a UD pattern. Conversely, the critical LTB load values are lower for the beam with the D2 pattern in comparison to the UD pattern.
2. The beam with the D1 pattern demonstrates greater resistance to buckling than the D4 pattern, making the former the optimal choice for enhancing the bearing capacity of orthotropic I-beams.
3. The LTB loads of orthotropic I-beams are observed to decrease with increases in web depth and porosity coefficients. An increase in the orthotropy ratio, flange slenderness ratio, flange-to-web thickness ratio, and span of the beam is observed to correspond with an increase in these loads.
4. The nonuniform distribution of porosity (D1 and D3), which decreases from the origin to the flanges, serves to enhance the lateral stability of I-beams because the flange has the maximum value of Young's and shear modulus.
5. The influence of nonuniform porosity patterns on the porous orthotropic I-beam's critical LTB load values increases as the flange slenderness ratio, flange-to-web thickness ratio, orthotropy ratio, web depth, and span of beam increase. The UD porosity pattern effect on the porous orthotropic I-beam's critical LTB load values is independent of the increasing above parameters.
6. The discrepancy in porosity effect between the nonuniform (D1, D2, D3) and uniform (UD) porosity distribution patterns is amplified as the beam span, orthotropy ratio, and flange-to-web thickness ratio increase. Conversely, it is observed to diminish as the web depth and flange slenderness ratio increase.

Funding No funding was received for conducting this study.

Declarations

Conflict of interest The authors declare that they have no known competing financial interests or personal relationships that could have appeared to influence the work reported in this paper.

References

1. Dahmani, L., Drizi, S.: Lateral torsional buckling of an eccentrically loaded channel section beam. Strength Mater. **47**(6), 912–916 (2015). https://doi.org/10.1007/s11223-015-9728-x
2. Bedon, C., Amadio, C.: Analytical and numerical assessment of the strengthening effect of structural sealant joints for the prediction of the ltb critical moment in laterally restrained glass beams. Mater. Struct. **49**(6), 2471–2492 (2016). https://doi.org/10.1617/s11527-015-0661-z
3. Derks, J.P.B.N.: Linear elastic lateral buckling (including shear deformation) and linear elastic lateral torsional buckling of composite beams -an analytical engineering approach. Heron **62**(1), 1–20 (2017)
4. Subramanian, L., Jeong, W.Y., Yellepeddi, R., White, D.W.: Assessment of i-section member ltb resistances considering experimental test data and practical inelastic buckling design calculations. Eng. J.-Am. Inst. Steel Constr. **55**(1), 15–44 (2018)
5. Subramanian, L., White, D.W.: Reassessment of the lateral torsional buckling resistance of i-section members: uniform-moment studies. J. Struct. Eng. **143**(3) (2017). https://doi.org/10.1061/(Asce)St.1943-541x.0001686
6. Jönsson, J., Müller, M.S., Gamst, C., Valeš, J., Kala, Z.: Investigation of European flexural and lateral torsional buckling interaction. J. Constr. Steel Res. **156**, 105–121 (2019). https://doi.org/10.1016/j.jcsr.2019.01.026
7. Sahraei, A., Mohareb, M.: Lateral torsional buckling analysis of moment resisting plane frames. Thin-Walled Struct. **134**, 233–254 (2019). https://doi.org/10.1016/j.tws.2018.10.006
8. Fortan, M., Rossi, B.: Lateral torsional buckling of welded stainless-steel i-profile beams: design and reliability. J. Struct. Eng. **146**(12) (2020). https://doi.org/10.1061/(Asce)St.1943-541x.0002830
9. Agüero, A., Baláž, I., Koleková, Y.: New method for metal beams sensitive to lateral torsional buckling with an equivalent geometrical ugli imperfection. Structures **29**, 1445–1462 (2021). https://doi.org/10.1016/j.istruc.2020.11.047
10. Rossi, A., Saito, D.H., Martins, C.H., de Souza, A.S.C.: The influence of structural imperfections on the ltb strength of i-beams. Structures **29**, 1173–1186 (2021). https://doi.org/10.1016/j.istruc.2020.11.020
11. Armouti, N.S.: Lateral torsional buckling of beams bent about their single axis of symmetry by fem with linear elements. ARPN J. Eng. Appl. Sci. **17**(3), 344–355 (2022)
12. de Carvalho, A.S., Rossi, A., Martins, C.H.: Assessment of lateral-torsional buckling in steel i-beams with sinusoidal web openings. Thin-Walled Struct. **175** (2022). https://doi.org/10.1016/j.tws.2022.109242
13. Soltani, M.: A novel approach for lateral buckling assessment of double tapered thin-walled laminated composite i-beams. Mech. Adv. Compos. Struct. **9**(1), 11–23 (2022). https://doi.org/10.22075/macs.2021.22105.1313
14. Stroetmann, R., Fominow, S.: Equivalent geometric imperfections for the ltb-design of members with i-sections. Steel Constr.-Des. Res. **15**(4), 213–228 (2022). https://doi.org/10.1002/stco.202200025
15. Belaid, T., Slimani, A., Ammari, F., Boukhalfa, D., Adman, R.: Formulation of the critical lateral buckling moment of steel beams under asymmetric loadings. Thin-Walled Struct. **182** (2023). https://doi.org/10.1016/j.tws.2022.110163
16. Düğenci, O.: Determination of bending and lateral-torsional buckling displacements in castellated and circular opening steel beams by image processing. Structures **56** (2023). https://doi.org/10.1016/j.istruc.2023.104942
17. Pandit, U.K., Mondal, G., Punera, D.: Lateral torsional buckling analysis of corrugated steel web girders using homogenization approach. J. Constr. Steel Res. **210** (2023). https://doi.org/10.1016/j.jcsr.2023.108099
18. Anirudh, B., Ganapathi, M., Anant, C., Polit, O.: A comprehensive analysis of porous graphene-reinforced curved beams by finite element approach using higher-order structural theory: bending, vibration and buckling. Compos. Struct. **222** (2019). https://doi.org/10.1016/j.compstruct.2019.110899
19. Barati, M.R., Zenkour, A.M.: Post-buckling analysis of refined shear deformable graphene platelet reinforced beams with porosities and geometrical imperfection. Compos. Struct. **181**, 194–202 (2017). https://doi.org/10.1016/j.compstruct.2017.08.082
20. Bridjesh, P., Geetha, N.K., Reddy, G.C.M.: On numerical investigation of buckling in two-directional porous functionally graded beam using higher order shear deformation theory. Mech. Adv. Compos. Struct. **10**(2), 393–406 (2023). https://doi.org/10.22075/macs.2023.29340.1462
21. Bridjesh, P., Geetha, N.K., Yelamasetti, B.: Numerical investigation on buckling of two-directional porous functionally graded beam using higher order shear deformation theory. Int. J. Interact. Des. Manuf. **21**(1), 109–119 (2023). https://doi.org/10.1007/s12008-023-01332-6
22. Chen, D., Rezaei, S., Rosendahl, P.L., Xu, B.X., Schneider, J.: Multiscale modelling of functionally graded porous beams: buckling and vibration analyses. Eng. Struct. **266** (2022). https://doi.org/10.1016/j.engstruct.2022.114568
23. Chen, D., Yang, J., Kitipornchai, S.: Elastic buckling and static bending of shear deformable functionally graded porous beam. Compos. Struct. **133**, 54–61 (2015). https://doi.org/10.1016/j.compstruct.2015.07.052
24. Ebrahimi, F., Barati, M.R.: Stability analysis of porous multi-phase nanocrystalline nonlocal beams based on a general higher-order couple-stress beam model. Struct. Eng. Mech. **65**(4), 465–476 (2018). https://doi.org/10.12989/sem.2018.65.4.465
25. Jamshidi, M., Arghavani, J.: Optimal design of two-dimensional porosity distribution in shear deformable functionally graded porous beams for stability analysis. Thin-Walled Struct. **120**, 81–90 (2017). https://doi.org/10.1016/j.tws.2017.08.027

26. Jamshidi, M., Arghavani, J.: Optimal material tailoring of functionally graded porous beams for buckling and free vibration behaviors. Mech. Res. Commun. **88**, 19–24 (2018). https://doi.org/10.1016/j.mechrescom.2018.01.006
27. Keleshteri, M.M., Jelovica, J.: Beam theory reformulation to implement various boundary conditions for generalized differential quadrature method. Eng. Struct. **252** (2022). https://doi.org/10.1016/j.engstruct.2021.113666
28. Liu, Y.J., Su, S.K., Huang, H.W., Liang, Y.J.: Thermal-mechanical coupling buckling analysis of porous functionally graded sandwich beams based on physical neutral plane. Compos. Part B-Eng. **168**, 236–242 (2019). https://doi.org/10.1016/j.compositesb.2018.12.063
29. Nguyen, N.D., Nguyen, T.N., Nguyen, T.K., Vo, T.P.: A Chebyshev–Ritz solution for size-dependent analysis of the porous microbeams with various boundary conditions. Int. J. Mech. Mater. Des. **19**(4), 861–881 (2023). https://doi.org/10.1007/s10999-023-09666-5
30. Sekkal, M., Bachir Bouiadjra, R., Benyoucef, S., Tounsi, A., Ghazwani, M.H., Alnujaie, A.: Investigation on static stability of bidirectional fg porous beams exposed to variable axial load. Acta Mech. **234**(3), 1239–1257 (2022). https://doi.org/10.1007/s00707-022-03370-9
31. Teng, Z.C., Wang, W.B., Gu, C.L.: Free vibration and buckling characteristics of porous functionally graded materials (fgms) micro-beams based on the modified couple stress theory. Zamm-Zeitschrift Fur Angew. Math. Und Mech. **102**(4) (2022). https://doi.org/10.1002/zamm.202100219
32. Alkhedher, M.: Hygrothermal environment effect on the critical buckling load of fgp microbeams with initial curvature integrated by cnt-reinforced skins considering the influence of thickness stretching. Nanotechnol. Rev. **10**(1), 1140–1156 (2021). https://doi.org/10.1515/ntrev-2021-0076
33. Bamdad, M., Mohammadimehr, M., Alambeigi, K.: Analysis of sandwich timoshenko porous beam with temperature-dependent material properties: magneto-electro-elastic vibration and buckling solution. J. Vib. Control **25**(23–24), 2875–2893 (2019). https://doi.org/10.1177/1077546319860314
34. Bamdad, M., Mohammadimehr, M., Alambeigi, K.: Bending and buckling analysis of sandwich reddy beam considering shape memory alloy wires and porosity resting on vlasov's foundation. Steel Compos. Struct. **36**(6), 671–687 (2020). https://doi.org/10.12989/scs.2020.36.6.671
35. Chen, X.H., Shen, H.S., Li, C.: Re-examination of nonlinear vibration, nonlinear bending and thermal postbuckling of porous sandwich beams reinforced by graphene platelets. Compos. Struct. **322** (2023). https://doi.org/10.1016/j.compstruct.2023.117392
36. Chinnapandi, L.B.M., Pitchaimani, J., Eltaher, M.A.: Vibro-acoustics of functionally graded porous beams subjected to thermo-mechanical loads. Steel Compos. Struct. **44**(6), 815–829 (2022). https://doi.org/10.12989/scs.2022.44.6.815
37. Dang, V.H., Nguyen, T.H.: Buckling and nonlinear vibration of functionally graded porous micro-beam resting on elastic foundation. Mech. Adv. Compos. Struct. **9**(1), 75–88 (2022). https://doi.org/10.22075/MACS.2021.24098.1350
38. Eiadtrong, S., Wattanasakulpong, N., Vo, T.P.: Thermal vibration of functionally graded porous beams with classical and non-classical boundary conditions using a modified fourier method. Acta Mech. **234**(2), 729–750 (2023). https://doi.org/10.1007/s00707-022-03401-5
39. Enayat, S., Hashemian, M., Toghraie, D., Jaberzadeh, E.: Bending, buckling and vibration analyses of fg porous nanobeams resting on pasternak foundation incorporating surface effects. Zamm-Zeitschrift Fur Angew. Math. Und Mech. (2020). https://doi.org/10.1002/zamm.202000231
40. Hanifehlou, S., Mohammadimehr, M.: Buckling analysis of sandwich beam reinforced by gpls using various shear deformation theories. Comput. Concrete **25**(5), 427–432 (2020). https://doi.org/10.12989/cac.2020.25.5.427
41. Jankowski, P., Zur, K.K., Kim, J., Reddy, J.N.: On the bifurcation buckling and vibration of porous nanobeams. Compos. Struct. **250** (2020). https://doi.org/10.1016/j.compstruct.2020.112632
42. Mollamahmutoğlu, Ç., Mercan, A., Levent, A.: A comprehensive mechanical response and dynamic stability analysis of elastically restrained bi-directional functionally graded porous microbeams in the thermal environment via mixed finite elements. J. Braz. Soc. Mech. Sci. Eng. **44**(8) (2022). https://doi.org/10.1007/s40430-022-03616-6
43. Patil, H.B., Pitchaimani, J., Mailan Chinnapandi, L.B.: Buckling and free vibration of porous functionally graded metal ceramic beams under thermal and mechanical loading: a comparative study. J. Inst. Eng. (India): Ser. C **102**(5), 1107–1117 (2021). https://doi.org/10.1007/s40032-021-00742-3
44. Polit, O., Anant, C., Anirudh, B., Ganapathi, M.: Functionally graded graphene reinforced porous nanocomposite curved beams: bending and elastic stability using a higher-order model with thickness stretch effect. Compos. Part B-Eng. **166**, 310–327 (2019). https://doi.org/10.1016/j.compositesb.2018.11.074
45. Xiao, W.S., Gao, Y., Zhu, H.P.: Buckling and post-buckling of magneto-electro-thermo-elastic functionally graded porous nanobeams. Microsyst. Technol.-Micro- Nanosyst.-Inf. Storage Process. Syst. **25**(6), 2451–2470 (2019). https://doi.org/10.1007/s00542-018-4145-2
46. Li, Q.L., Zhang, H.K.: Influence of surface effect on post-buckling behavior of graded porous nanobeam subjected to follower force. Microsyst. Technol.-Micro- Nanosyst.-Inf. Storage Process. Syst. **29**(5), 779–791 (2023). https://doi.org/10.1007/s00542-023-05458-1
47. Phan, T.-B., Nguyen, N.-D.: Buckling and free vibration analysis of functionally graded porous beams using a higher-order deformation theory. In: Computational Intelligence Methods for Green Technology and Sustainable Development (pp. 446–460, Vol. 567 LNNS) (2023). https://doi.org/10.1007/978-3-031-19694-2_40
48. Turan, M., Adiyaman, G.: Free vibration and buckling analysis of porous two-directional functionally graded beams using a higher-order finite element model. J. Vib. Eng. Technol. **12**(1), 1133–1152 (2024). https://doi.org/10.1007/s42417-023-00898-5
49. Wang, S.Y., Li, Q.L.: Thermoelastic dynamic responses near buckling of the non-conservative gradient porous beam in hygrothermal environments. J. Vib. Eng. Technol. **12**(1), 1049–1066 (2024). https://doi.org/10.1007/s42417-023-00893-w
50. Zhang, Q., Sun, Y.X.: Buckling and post-buckling of bidirectional porous beam under bidirectional hygrothermal environment. Int. J. Struct. Stab. Dyn. **24**(02) (2024). https://doi.org/10.1142/S0219455424500202
51. Song, J.-P., She, G.-L.: Nonlinear resonance and chaotic dynamic of rotating graphene platelets reinforced metal foams plates in thermal environment. Arch. Civil Mech. Eng. **24**(1), 1–31 (2024). https://doi.org/10.1007/s43452-023-00846-w

52. Zhang, Y.-W., She, G.-L.: Combined resonance of graphene platelets reinforced metal foams cylindrical shells with spinning motion under nonlinear forced vibration. Eng. Struct. **300**, 1–23 (2024). https://doi.org/10.1016/j.engstruct.2023.117177
53. Ziane, N., Meftah, S.A., Ruta, G., Tounsi, A.: Thermal effects on the instabilities of porous fgm box beams. Eng. Struct. **134**, 150–158 (2017). https://doi.org/10.1016/j.engstruct.2016.12.039
54. Liu, L., Liu, A., Yang, J., Fu, J.: Lateral-torsional buckling of functionally graded porous arches with graphene platelets reinforcements under an arbitrary radial concentrated load. Compos. Struct. **281** (2022). https://doi.org/10.1016/j.compstruct.2021.114973
55. Benyamina, A.B., Meftah, S.A., Mohri, F., Daya, E.M.: Analytical solutions attempt for lateral torsional buckling of doubly symmetric web-tapered i-beams. Eng. Struct. **56**, 1207–1219 (2013). https://doi.org/10.1016/j.engstruct.2013.06.036
56. Mohri, F., Azrar, L., Potier-Ferry, M.: Lateral post-buckling analysis of thin-walled open section beams. Thin-Walled Struct. **40**(12), 1013–1036 (2002). https://doi.org/10.1016/S0263-8231(02)00043-5
57. Sapountzakis, E.J., Dourakopoulos, J.A.: Lateral buckling analysis of beams of arbitrary cross section by bem. Comput. Mech. **45**(1), 11–21 (2009). https://doi.org/10.1007/s00466-009-0416-1
58. Eurocode-3.: Eurocode 3–design of steel structures. BS EN **1**(1), 2005 (1993)

Publisher's Note Springer Nature remains neutral with regard to jurisdictional claims in published maps and institutional affiliations.

Springer Nature or its licensor (e.g. a society or other partner) holds exclusive rights to this article under a publishing agreement with the author(s) or other rightsholder(s); author self-archiving of the accepted manuscript version of this article is solely governed by the terms of such publishing agreement and applicable law.